

Time-resolved IR Studies on the Mechanism for the  
Functionalization of Primary C–H Bonds by Photoactivated  
Cp\*W(CO)<sub>3</sub>(Bpin)Karma R. Sawyer,<sup>†,‡,§</sup> James F. Cahoon,<sup>†,‡,¶</sup> Jennifer E. Shanoski,<sup>†,‡,△</sup>  
Elizabeth A. Glascoe,<sup>†,‡,▲</sup> Matthias F. Kling,<sup>†,‡,○</sup> Jacob P. Schlegel,<sup>†,‡</sup>  
Matthew C. Zoerb,<sup>†,‡</sup> Marko Hapke,<sup>‡,●</sup> John F. Hartwig,<sup>\*,‡,§</sup>  
Charles Edwin Webster,<sup>\*,‡,||</sup> and Charles B. Harris<sup>\*,†,‡</sup>

Department of Chemistry, University of California, Berkeley, California 94720, Department of  
Chemistry, Yale University, New Haven, Connecticut 06520, Department of Chemistry,  
University of Illinois, Urbana, Illinois 61801, Department of Chemistry, The University of  
Memphis, Memphis, Tennessee 38152, and Chemical Sciences Division, Lawrence Berkeley  
National Laboratory, Berkeley, California 94720

Received July 30, 2009; E-mail: cbharris@berkeley.edu; cewebstr@memphis.edu; jhartwig@scs.uiuc.edu

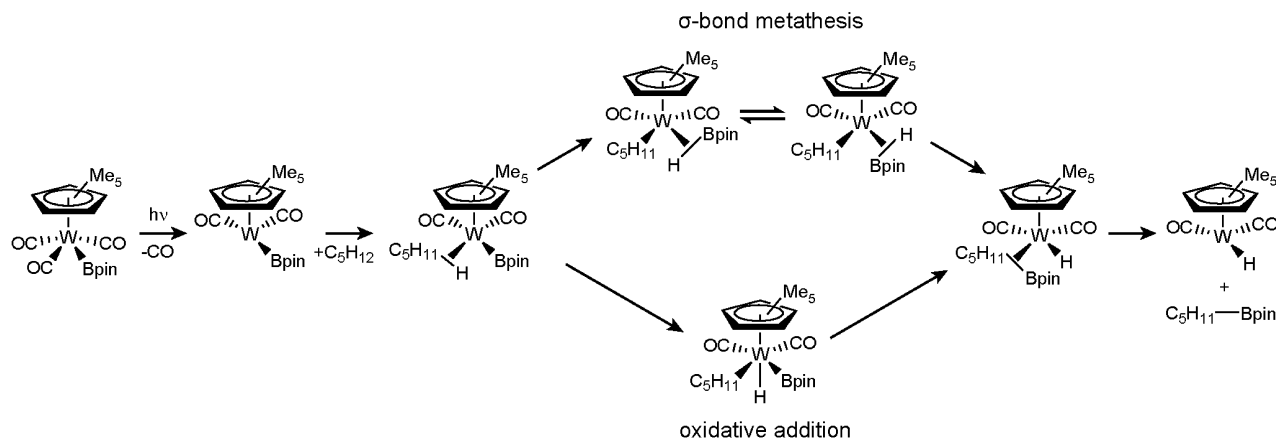
**Abstract:** Recently, transition-metal–boryl compounds have been reported that selectively functionalize primary C–H bonds in alkanes in high yield. We have investigated this process with one of the well-defined systems that reacts under photochemical conditions using both density functional theory calculations and pico- through microsecond time-resolved IR spectroscopy. UV irradiation of Cp\*W(CO)<sub>3</sub>(Bpin) (Cp\* = C<sub>5</sub>(CH<sub>3</sub>)<sub>5</sub>; pin = 1,2-O<sub>2</sub>C<sub>2</sub>-(CH<sub>3</sub>)<sub>4</sub>) in neat pentane solution primarily results in dissociation of a single CO ligand and solvation of the metal by a pentane molecule from the bath within 2 ps. The spectroscopic data imply that the resulting complex, *cis*-Cp\*W(CO)<sub>2</sub>(Bpin)(pentane), undergoes C–H bond activation by a  $\sigma$ -bond metathesis mechanism—in 16  $\mu$ s, a terminal hydrogen on pentane appears to migrate to the Bpin ligand to form a  $\sigma$ -borane complex, Cp\*W(CO)<sub>2</sub>(H-Bpin)(C<sub>5</sub>H<sub>11</sub>). Our data imply that the borane ligand rotates until the boron is directly adjacent to the C<sub>5</sub>H<sub>11</sub> ligand. In this configuration, the B–H  $\sigma$ -bond is broken in favor of a B–C  $\sigma$ -bond, forming Cp\*W(CO)<sub>2</sub>(H)(C<sub>5</sub>H<sub>11</sub>-Bpin), a tungsten–hydride complex containing a weakly bound alkylboronate ester. The ester is then eliminated to form Cp\*W(CO)<sub>2</sub>(H) in approximately 170  $\mu$ s. We also identify two side reactions that limit the total yield of bond activation products and explain the 72% yield previously reported for this complex.

## 1. Introduction

The functionalization of the strong C–H bonds in saturated alkanes presents an enormous challenge that has been the focus of extensive research effort over the past 50 years.<sup>1–6</sup> It has long been known that transition-metal complexes can function-

alize C–H bonds of alkane solvents at room temperature, but the reactions are generally not selective for a specific type of C–H bond.<sup>7</sup> Recently, however, one of the authors' laboratories discovered transition-metal–boryl complexes that selectively<sup>2,6,8–10</sup> functionalize primary C–H bonds by both thermal<sup>2,8</sup> and photochemical<sup>6,9,10</sup> reactions with yields as high as 92%. The mechanism of C–H bond cleavage and functionalization by these compounds has been investigated experimentally<sup>2,6,8–10</sup> and theoretically,<sup>8,11,12</sup> but complexes proposed to be intermediates have not been observed previously by spectroscopic

<sup>†</sup> University of California, Berkeley.<sup>‡</sup> Yale University.<sup>§</sup> University of Illinois.<sup>||</sup> The University of Memphis.<sup>△</sup> Lawrence Berkeley National Laboratory.<sup>¶</sup> Present address: Department of Mechanical Engineering, 4164 Etcheverry Hall, University of California, Berkeley, CA 94720.<sup>○</sup> Present address: Department of Chemistry and Chemical Biology, Harvard University, Cambridge, MA 02138.<sup>▲</sup> Present address: Department of Chemistry, Merritt College, Oakland, CA 94619.<sup>●</sup> Present address: Lawrence Livermore National Laboratory, 7000 East Ave., Livermore, CA 94550.<sup>○</sup> Present address: Max-Planck Institute of Quantum Optics, Hans-Kopfermann-Str. 1, 85748, Garching, Germany.<sup>●</sup> Present address: Leibniz-Institut für Katalyse, A.-Einstein-Str. 29A, D-18059, Rostock, Germany.(1) Bromberg, S. E.; Yang, H.; Asplund, M. C.; Lian, T.; McNamara, B. K.; Kotz, K. T.; Yeston, J. S.; Wilkens, M.; Frei, H.; Bergman, R. G.; Harris, C. B. *Science* **1997**, 278, 260–263.(2) Chen, H.; Schlecht, S.; Semple, T. C.; Hartwig, J. F. *Science* **2000**, 287, 1995–1997.(3) Cowan, A. J.; Portius, P.; Kawanami, K.; Jina, O. S.; Grills, D. C.; Sun, X.; McMaster, J.; George, M. W. *Proc. Natl. Acad. Sci. U.S.A.* **2007**, 104, 6933–6938.(4) Crabtree, R. H. *The Organometallic Chemistry of Transition Metals*; John Wiley & Sons: New York, 2001.(5) Trushin, S.; Fuss, W.; Kompa, K. L.; Schmid, W. *J. Phys. Chem. A* **2000**, 259, 1997–2006.(6) Waltz, K. M.; Hartwig, J. F. *Science* **1997**, 277, 211–213.(7) Shilov, A. E.; Shul'pin, G. B. *Chem. Rev.* **1997**, 97, 2879–2932.(8) Hartwig, J. F.; Cook, K. S.; Hapke, M.; Incarvito, C. D.; Fan, Y.; Webster, C. E.; Hall, M. B. *J. Am. Chem. Soc.* **2005**, 127, 2538–2552.(9) Waltz, K. M.; Hartwig, J. F. *J. Am. Chem. Soc.* **2000**, 122, 11358–11369.(10) Waltz, K. M.; Muhoro, C. N.; Hartwig, J. F. *Organometallics* **1999**, 18, 3383–3393.

**Scheme 1.** Proposed Mechanisms for the C–H Bond Activation by Photoactivated Tungsten–Boryl Complexes in Neat Pentane Solution:  $\sigma$ -Bond Metathesis and Oxidative Addition

methods. In this study, we use pico- through microsecond time-resolved IR spectroscopy and density functional theory (DFT) calculations to identify these intermediates and determine the sequential steps in the mechanism for the functionalization of primary C–H bonds in aliphatic substrates to alkylboronate esters by  $\text{Cp}^*\text{W}(\text{CO})_3(\text{Bpin})$  under photochemical conditions.<sup>8,11,12</sup>

Scheme 1 shows two mechanisms that have been proposed for this reaction.<sup>8,9,11,12</sup> Both pathways begin with CO photodissociation from the starting material to form  $\text{Cp}^*\text{W}(\text{CO})_2(\text{Bpin})$ , which is solvated by a pentane molecule from the bath. In the  $\sigma$ -bond metathesis mechanism, the solvated complex reacts to form a W(II)  $\sigma$ -borane intermediate,  $\text{Cp}^*\text{W}(\text{CO})_2(\text{H-Bpin})(\text{C}_5\text{H}_{11})$ , which can adopt a structure in which either the hydrogen or the boron of the Bpin group is adjacent to the  $\text{C}_5\text{H}_{11}$  group. In the oxidative addition mechanism, the alkane adds to the metal center to form a discrete W(IV) intermediate,  $\text{Cp}^*\text{W}(\text{CO})_2(\text{Bpin})(\text{H})(\text{C}_5\text{H}_{11})$ . In both pathways, a strong B–C bond forms between the  $\text{C}_5\text{H}_{11}$  group and the Bpin group in the next step to form an initial product  $\text{Cp}^*\text{W}(\text{CO})_2(\text{H})(\text{H}_{11}\text{C}_5\text{-Bpin})$ , containing a hydride ligand and a coordinated alkylboronate ester. The alkylboronate ester then dissociates in the final step of the reaction to form the free organic product and the unsaturated metal hydride complex  $\text{Cp}^*\text{W}(\text{CO})_2(\text{H})$ .

The mechanisms for both pathways have been investigated in previous DFT studies, and these studies indicate that both pathways are accessible at room temperature.<sup>11,12</sup> Initially, the oxidative addition mechanism was considered more favorable because it is a common mechanism for C–H bond activation by mid- to late-transition-metal complexes, such as  $[\text{Cp}^*\text{Ir}(\text{PMe}_3)(\text{CH}_3)]^+$  and  $\text{Tp}^*\text{Rh}(\text{CO})_2$  ( $\text{Tp}^* = \text{HB-Pz}_3^*$  where  $\text{Pz}^* = 3,5\text{-dimethylpyrazolyl}$ ).<sup>1,13</sup> Similarly, the  $\sigma$ -bond metathesis mechanism was considered less likely because it occurs more commonly with high-valent early transition-metal complexes, and the tungsten–boryl complex that produced the highest yields of functionalized product is low-valent.<sup>6,9,12</sup> Nevertheless, the most recent DFT studies predict that the  $\sigma$ -bond metathesis mechanism is the lower energy pathway.<sup>8,11,12,14</sup>

The goal of this study has been to use a combination of time-resolved IR spectroscopy and DFT calculations to probe the identity and rates of reactions of intermediates in the C–H bond functionalization of alkanes by photoactivated metal–boryl complexes. These techniques have been shown to be effective for assessing the mechanisms of other bond activation processes by transition-metal complexes.<sup>4,13,15–17</sup> Here we report the direct spectroscopic observation of complexes that we assign by a set of experimental and computational methods to be intermediates formed during a  $\sigma$ -bond metathesis mechanism for the C–H borylation process. In addition, we have identified two side reactions that limit the yield of bond activation products.

## 2. Methods

**2.1. Synthesis of  $\text{Cp}^*\text{W}(\text{CO})_3(\text{Bpin})$ .**  $\text{Cp}^*\text{W}(\text{CO})_3(\text{Bpin})$  was synthesized by a published procedure.<sup>6,9,10</sup> In brief, a 1.0 M solution of  $\text{BCl}_3$  in heptane was added via syringe to a vigorously stirred solution of pinacol in pentane at 0 °C. Afterward, the reaction was stirred at room temperature for 1 h, and the solution was condensed under vacuum until a few milliliters of liquid remained in the flask. The mixture was filtered to remove white insoluble impurities and was used immediately to avoid thermal decomposition. The crude pentane solution of  $\text{ClBpin}$  was added to a stirred suspension of  $\text{LiCp}^*\text{W}(\text{CO})_3$  in pentane. The mixture was stirred for 45 min and then filtered to remove all solid material. The pentane solution was condensed under vacuum. Four recrystallizations at –30 °C were performed to remove impurities, affording a pure, pale yellow transition-metal–boryl complex. The compound was stored and handled under nitrogen atmosphere in a glovebox (Vacuum Atmospheres Company). For experiments, dilute solutions, ~5 mM with an IR optical density of 0.7, were prepared in neat pentane, and the air-sensitive solutions were maintained under positive argon pressure.

**2.2. Ultrafast Time-Resolved Infrared Spectroscopy.** The ultrafast experimental setup has been described in detail elsewhere.<sup>16,18,19</sup> A Ti:sapphire regenerative amplifier seeded by a Ti:sapphire oscillator is used to produce a 1 kHz train of 100 fs pulses centered at 800 nm. The output is split so that 30% is used for the

(11) Webster, C. E.; Fan, Y.; Hall, M. B.; Kunz, D.; Hartwig, J. F. *J. Am. Chem. Soc.* **2003**, *125*, 858–859.

(12) Lam, W. H.; Lin, Z. *Organometallics* **2003**, *22*, 473–480.

(13) Arndtsen, B. A.; Bergman, R. G. *Science* **1995**, *270*, 1970–1973.

(14) Our unpublished DFT studies also show that a  $\sigma$ -bond metathesis mechanism in which the B–C bond is formed directly without formation of a metal–alkyl intermediate has too high a barrier to be a feasible pathway.

(15) (a) Asplund, M. C.; Snee, P. T.; Yeston, J. S.; Wilkens, M. J.; Payne, C. K.; Yang, H.; Kotz, K. T.; Frei, H.; Bergman, R. G.; Harris, C. B. *J. Am. Chem. Soc.* **2002**, *124*, 10605–10612. (b) Blake, A. J.; George, M. W.; Hall, M. B.; McMaster, J.; Portius, P.; Sun, X. Z.; Webster, C. E.; Wilson, C.; Zaric, S. D. *Organometallics* **2008**, *27*, 189–201.

(16) Glascoe, E. A.; Sawyer, K. R.; Shanoski, J. E.; Harris, C. B. *J. Phys. Chem. C* **2007**, *111*, 8789–8795.

(17) Lian, T.; Bromberg, S. E.; Asplund, M. C.; Yang, H.; Harris, C. B. *J. Phys. Chem.* **1996**, *100*, 11994–12001.

generation of the 266 nm pump pulses, which are stretched to  $\sim 1$  ps to utilize relatively high pump powers and signal-to-noise ratios without forming products from multiphoton absorption. Additionally, spectra were measured at a variety of pump powers to verify that the utilized pump energies did not generate multiphoton products. Typically, 5–7  $\mu\text{J}$  of 266 nm light is measured at the sample. The remainder of the regenerative amplifier output is used to pump a home-built OPA that is tunable from 3.0–6.0  $\mu\text{m}$  and has a spectral width of ca. 200  $\text{cm}^{-1}$ . The mid-IR light is split to create IR-pump, IR-probe, and reference lines. Two computer-controlled translation stages are used to create time delays between the IR-pump and IR-probe pulses (up to ca. 300 ps) and the UV-pump and IR-probe pulses (up to ca. 3 ns). The polarizations of both pump pulses are set relative to the polarization of the IR-probe using a zero-order half-wave plate. The IR-probe pulse is focused and spatially overlapped with the focused UV- and IR-pump pulses at the sample cell, which is fitted with 2.0 mm thick  $\text{CaF}_2$  windows for an optical path length of 250  $\mu\text{m}$ . For the UV-pump experiments, the sample solution is mechanically pumped through the cell, and the cell itself is moved by computer-controlled translational stages in the sample plane after each measured spectrum. IR-probe and reference beams are sent through a computer-controlled spectrograph and are detected by a  $2 \times 32$  element MCT array IR detector with a spectral resolution of ca. 3  $\text{cm}^{-1}$ . The signals are averaged over 1000 laser shots to account for shot-to-shot fluctuations. Differences in optical density as small as  $5 \times 10^{-5}$  are observable after 1 s of data collection. The Levenberg–Marquardt method was used to fit the kinetic data to sums of exponentials convoluted with a Gaussian (fwhm = 1.1 ps). Errors in the kinetic data are reported at 95% confidence intervals.

**2.3. Nano- through Microsecond Step-Scan FTIR Spectroscopy.** The experimental setup of the step-scan FTIR apparatus has been described in detail elsewhere.<sup>20</sup> In brief, for experiments in the 1700–2100  $\text{cm}^{-1}$  region with a spectral resolution of ca. 4  $\text{cm}^{-1}$ , a HgCdTe PV detector KMPV8-1-J2 (fwhm = 37 ns, RC decay of AC amplifier = 1.4 ms) was employed. AC-coupled and DC-coupled interferometric signals were simultaneously acquired by a 40 MHz, 12-bit digitizer (model PAD 1232). Samples were photolyzed with 25 ns pulses of the fourth harmonic of a Nd:YAG laser (DCR2A, GCR-3 optics) at 266 nm. Photolysis light was aligned in a nearly collinear geometry ( $10^\circ$ ) with the infrared beam. To prevent scattered 266 nm light from reaching the interferometer and detector optics, anti-reflection-coated Ge plates (International Scientific, 95% transmittance) were placed in the openings of the interferometer and detector compartments. Data acquisition was triggered by a small fraction of the photolysis laser pulse detected with an EG&G silicon photodiode (SGD-444). A similar sample cell that was employed in the ultrafast UV-pump, IR-probe experiments was used. Data were typically averaged over 15 laser-induced decays recorded for each mirror position of the step-scan apparatus, and 5–10 full time-resolved step-scan experiments were performed on each sample to ensure reproducibility and to allow for statistical analysis of data. Typically, changes in optical density of  $5 \times 10^{-5}$  were resolvable in these experiments. Again, time constants for chemical reactions were determined by fitting the kinetics to a sum of exponentials using the Levenberg–Marquardt method, and all errors correspond to a 95% confidence interval.

**2.4. Density Functional Theory (DFT) Calculations.** Theoretical calculations have been carried out using the Gaussian03<sup>21</sup> implementation of B3LYP (the B3 exchange functional<sup>22</sup> and LYP correlation functional)<sup>23</sup> and BVP86 (the Becke exchange functional (B)<sup>24</sup> and the Perdew correlation functional (VP86))<sup>25</sup> density functional theory,<sup>26</sup> using the default pruned fine grids for energies (75, 302), default pruned course grids for gradients and Hessians (35, 110) (neither grid is pruned for tungsten), and default SCF convergence for geometry optimizations ( $10^{-8}$ ). BVP86 will hereafter be referred to as BP86. To ease computational expense, either methane or propane molecules were used in place of the pentane ligand used experimentally. Shortening alkane ligands is a common method for reducing computational expense.<sup>11,12,27,28</sup> The B3LYP functional has been shown typically to provide reasonable and reliable results for many systems containing transition metals, including organometallic systems,<sup>29–31</sup> although there are exceptions.<sup>32</sup> Solvent effects on spectral shifts are well-known.<sup>33</sup> In the current study, the expected small shifts from nonspecific solvation are assumed to be similar for the various computed stationary points, and no methods for treating implicit solvent effects were included in the calculations.

All calculations were conducted with the same basis set combination. The basis set for tungsten (341/341/21) was the Hay and Wadt basis set and effective core potential (ECP) combination (LANL2DZ)<sup>34</sup> as modified by Couty and Hall, where the two outermost  $p$  functions have been replaced by a (41) split of the optimized tungsten  $6p$  function.<sup>35</sup> The cc-pVDZ basis sets<sup>36</sup> were used for all metal-ligated atoms, borons, and oxygens. Each cc-pVDZ basis set has had the redundant functions removed and has been linearly transformed, as suggested by Davidson.<sup>37</sup> All other atoms utilized the D95 basis sets.<sup>38</sup> The density fitting approximation<sup>39</sup> for the fitting of the Coulomb potential was used for all BP86 calculations when methane was utilized as the alkane; auxiliary density-fitting basis functions were generated automatically (by the procedure implemented in Gaussian 03) for the specified AO basis

- (18) Cahoon, J. F.; Kling, M. F.; Schmatz, S.; Harris, C. B. *J. Am. Chem. Soc.* **2005**, *127*, 12555–12565. Sawyer, K. R.; Steele, R. P.; Glascoe, E. A.; Cahoon, J. F.; Schlegel, J. P.; Head-Gordon, M.; Harris, C. B. *J. Phys. Chem. A* **2008**, *112*, 8505–8514.
- (19) (a) Shanoski, J. E.; Glascoe, E. A.; Harris, C. B. *J. Phys. Chem. B* **2006**, *110*, 996–1005. (b) Sawyer, K. R.; Glascoe, E. A.; Cahoon, J. F.; Schlegel, J. P.; Harris, C. B. *Organometallics* **2008**, *27*, 4370–4379. (c) Cahoon, J. F.; Sawyer, K. R.; Schlegel, J. P.; Harris, C. B. *Science* **2008**, *319*, 1820–1823.
- (20) (a) Sun, H.; Frei, H. *J. Phys. Chem. B* **1997**, *101*, 205–209. (b) Yeom, Y.; Frei, H. *J. Phys. Chem. B* **2003**, *107*, 6286–6291.

- (21) Frisch M. J. *Gaussian 03*, revision C.02; Gaussian, Inc.: Wallingford, CT, 2004.
- (22) Becke, A. D. *J. Chem. Phys.* **1993**, *98*, 5648.
- (23) Lee, C.; Yang, W.; Parr, R. G. *Phys. Rev. B* **1988**, *37*, 785.
- (24) Becke, A. D. *Phys. Rev. A* **1988**, *38*, 3098.
- (25) (a) Perdew, J. P. *Phys. Rev. B* **1986**, *33*, 8822–8824. (b) Perdew, J. P.; Zunger, A. *Phys. Rev. B* **1981**, *23*, 5048–5079.
- (26) Parr, R. G.; Yang, W. *Density Functional Theory of Atoms and Molecules*; Oxford University Press: New York, 1989.
- (27) (a) Cedeno, D. L.; Weitz, E. *Organometallics* **2003**, *22*, 2652. (b) Glascoe, E. A.; Kling, M. F.; Shanoski, J. E.; DiStasio, R. A., Jr.; Payne, C. K.; Mork, B. V.; Tilley, T. D.; Harris, C. B. *Organometallics* **2007**, *26*, 1424–1432.
- (28) (a) Snee, P. T.; Payne, C. K.; Kotz, K. T.; Yang, H.; Harris, C. B. *J. Am. Chem. Soc.* **2001**, *123*, 2255–2264. (b) Snee, P. T.; Yang, H.; Kotz, K. T.; Payne, C. K.; Harris, C. B. *J. Phys. Chem. A* **1999**, *103*, 10426.
- (29) Niu, S.; Hall, M. B. *Chem. Rev.* **2000**, *100*, 353–406.
- (30) (a) Nowlan, D. T.; Gregg, T. M.; Davies, H. M. L.; Singleton, D. A. *J. Am. Chem. Soc.* **2003**, *125*, 15902–15911. (b) Siegbahn, P. E. M. *J. Biol. Inorg. Chem.* **2006**, *11*, 695–701. (c) Siegbahn, P. E. M.; Tye, J. W.; Hall, M. B. *Chem. Rev.* **2007**, *107*, 4414–4435. (d) Riley, K. E.; Merz, K. M. *J. Phys. Chem. A* **2007**, *111*, 6044–6053. (e) Rinaldo, D.; Tian, L.; Harvey, J. N.; Friesner, R. A. *J. Chem. Phys.* **2008**, *129*, 164108.
- (31) Vastine, B. A.; Hall, M. B. *J. Am. Chem. Soc.* **2007**, *129*, 12068–12069.
- (32) DeYonker, N. J.; Williams, T. G.; Imel, A. E.; Cundari, T. R.; Wilson, A. K. *J. Chem. Phys.* **2009**, *131*, 024106.
- (33) (a) Drago, R. S. *Applications of Electrostatic-Covalent Models in Chemistry*; Surfside Publishers: Gainesville, FL, 1994. (b) Reichardt, C. *Solvents and Solvent Effects in Organic Chemistry*; Wiley-VCH: New York, 2003.
- (34) (a) Hay, P. J.; Wadt, W. R. *J. Chem. Phys.* **1985**, *82*, 299–310. (b) Wadt, W. R.; Hay, P. J. *J. Chem. Phys.* **1985**, *82*, 284–298.
- (35) Couty, M.; Hall, M. B. *J. Comput. Chem.* **1996**, *17*, 1359–1370.
- (36) (a) Dunning, T. H. *J. Chem. Phys.* **1989**, *90*, 1007–1023. (b) Woon, D. E.; Dunning, T. H. *J. Chem. Phys.* **1994**, *100*, 2875–2988.
- (37) Davidson, E. R. *Chem. Phys. Lett.* **1996**, *260*, 514–518.



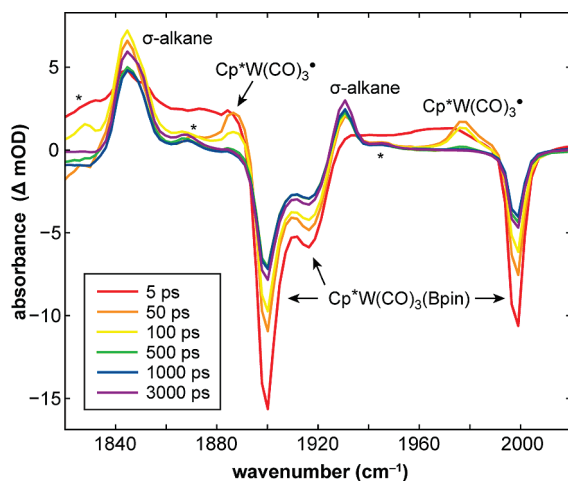


**Figure 1.** UV-pump, IR-probe spectra of  $\text{Cp}^*\text{W}(\text{CO})_3(\text{Bpin})$  in neat pentane solution. The features marked with \* are minor side products that are discussed in the Supporting Information.<sup>44</sup>

set. Spherical harmonic  $d$  functions were used throughout; that is, there are five angular basis functions per  $d$  function. Full ligands (except pentane for which methane or propane was substituted) were used in all computations. All structures were fully optimized, and analytical frequency calculations were performed on all structures to ensure either a zeroth-order saddle point (a local minimum) or a first-order saddle point (transition state: TS) was achieved.<sup>40</sup> All energies, enthalpies, and Gibbs free energies reported have been calculated using the B3LYP functional, and the vibrational frequencies reported have been calculated using the BP86 functional and have not been scaled.<sup>18,27,41</sup> Due to a fortuitous cancellation of errors, the absolute value of computed harmonic BP86/BVP86 stretching frequencies often compares favorably with experimental stretching frequencies that include anharmonicity—the BP86/BVP86 functionals underestimate the harmonic force constant when compared to experiment ( $\omega_c$ ).<sup>42</sup> The results from both B3LYP and BP86 give similar relative shifts for the computed IR frequencies.

### 3. Experimental Results

**3.1. Picosecond Dynamics.** Figure 1 shows UV-pump, IR-probe spectra of  $\text{Cp}^*\text{W}(\text{CO})_3(\text{Bpin})$  in neat pentane solution measured at time delays ranging from 5 to 3000 ps. The three negative features (referred to as parent bleaches) are centered at 1899, 1914, and 2000  $\text{cm}^{-1}$  and are due to the depletion of the reactant by the UV-pump pulse. The positive features are due to species formed as a result of the UV-pump pulse. Peak assignments are based on observed dynamics, literature,<sup>43</sup> and calculated CO vibrational frequencies. The intensities of the parent bleaches in Figure 1 rise on two time scales, an average fast time scale of  $35 \pm 11$  ps and

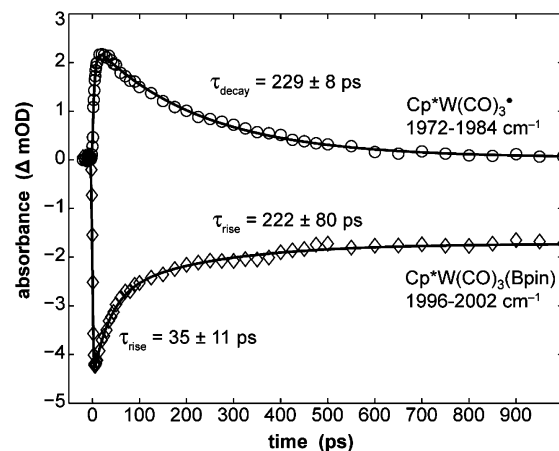


**Figure 2.** Kinetic plots for the  $\text{Cp}^*\text{W}(\text{CO})_3(\text{Bpin})$  and  $\text{Cp}^*\text{W}(\text{CO})_3\bullet$  features.

an average slow time scale of  $222 \pm 80$  ps, as shown in a kinetic plot of the 2000  $\text{cm}^{-1}$  bleach in Figure 2. Table 1 presents the dynamics of the individual spectral features. The fast recovery of the bleach is due to the cooling of reactant molecules that have been left vibrationally excited by the UV-pump pulse. This explanation is corroborated by ultrafast IR-pump, IR-probe measurements of the reactant (refer to Supporting Information), which indicate that this molecule undergoes vibrational relaxation in ca. 35 ps.

The 1888 and 1978  $\text{cm}^{-1}$  peaks are assigned to the  $\text{Cp}^*\text{W}(\text{CO})_3\bullet$  radical, which is produced by photodissociation of  $\bullet\text{Bpin}$  from the reactant.<sup>43</sup> These peaks decay on a time scale of  $229 \pm 8$  ps, which is similar to that of the slow rise of the bleaches (Figure 2). These similar time scales indicate that  $\text{Cp}^*\text{W}(\text{CO})_3\bullet$  recombines with  $\bullet\text{Bpin}$  in ca. 200 ps. The radical recombination is remarkably efficient—the peaks assigned to  $\text{Cp}^*\text{W}(\text{CO})_3\bullet$  decay to zero within experimental noise. It is unlikely that  $[\text{Cp}^*\text{W}(\text{CO})_3]_2$  is formed from the two radical species because dimerization will be limited by diffusion of the complexes out of their primary solvent shells, and this generally occurs on the microsecond time scale.<sup>45</sup> Furthermore, we do not observe the known vibrational peaks for the dimer.<sup>46</sup> These data imply that neither  $\text{Cp}^*\text{W}(\text{CO})_3\bullet$  nor  $\bullet\text{Bpin}$  is involved in C–H bond activation, a conclusion that agrees with past investigations.<sup>6,9–11</sup>

Previous experimental and computational studies, instead, showed that bond activation begins with the photodissociation of a CO from the reactant and subsequent solvation of the coordinatively unsaturated complex with an alkane molecule from the bath.<sup>6,9–12</sup> Generally, CO photodissociation occurs in less than 200 fs, and solvation occurs in 1–2 ps.<sup>5,17,48,49</sup> Therefore, we assign the remaining features centered at 1844 and 1931  $\text{cm}^{-1}$  to the  $\sigma$ -alkane complex,  $\text{Cp}^*\text{W}(\text{CO})_2(\text{Bpin})(\text{C}_5\text{H}_{12})$ . Upon close examination of the 1844  $\text{cm}^{-1}$  feature, however, it appears that there are actually two overlapping peaks in this spectral region. Panels A and B of Figure 3 show an enlargement of the feature at 2 and 1000 ps, respectively, along with a fit of the feature to Lorentzian functions.

(38) Dunning, T. H.; Hay, P. J. In *Modern Theoretical Chemistry*; Schaefer, H. F., III, Ed.; Plenum: New York, 1976.

(39) (a) Dunlap, B. I. *J. Chem. Phys.* **1983**, *78*, 3140–3142. (b) Dunlap, B. I. *J. Mol. Struct.* **2000**, *529*, 37–40. (c) Dunlap, B. I.; Connolly, J. W. D.; Sabin, J. R. *Chem. Phys.* **1979**, *71*, 3396–3402. (d) Dunlap, B. I.; Connolly, J. W. D.; Sabin, J. R. *J. Chem. Phys.* **1979**, *71*, 4993–4999.

(40) The computed frequencies for  $\text{Cp}^*\text{W}(\text{CO})_2(\text{HBpin})(\text{C}_3\text{H}_7)$  (Bpin-front) may have a slightly higher relative error than the computed frequencies for other minima because this minimum is extremely shallow.

(41) Scott, A. P.; Radom, L. *J. Phys. Chem.* **1996**, *100*, 16502–16513.  
(42) (a) Neugebauer, J.; Hess, B. A. *J. Chem. Phys.* **2003**, *118*, 7215–7225. (b) Jonas, V.; Thiel, W. *J. Phys. Chem. A* **1999**, *103*, 1381–1393. (c) Jonas, V.; Thiel, W. *Organometallics* **1998**, *17*, 353–360. (d) Jonas, V.; Thiel, W. *J. Chem. Phys.* **1996**, *105*, 3636–3648. (e) Jonas, V.; Thiel, W. *J. Chem. Phys.* **1995**, *105*, 8474–8484.

(43) Chong, T. S.; Li, P.; Leong, W. K.; Fan, W. Y. *J. Organomet. Chem.* **2005**, *690*, 4132–4138.

(44) The minor side products observed in the ultrafast spectra likely contribute to the decreased yield of the final product. However, we expect the contribution to be minor since the spectral features are low intensity.

(45) Desrosiers, M.; Wink, D.; Trautman, R.; Friedman, A.; Ford, P. *J. Am. Chem. Soc.* **1986**, *108*, 1917–1927.

(46) King, R. B.; Iqbal, M. Z.; King, A. D., Jr. *J. Organomet. Chem.* **1979**, *171*, 53–63.

(47) Steinfeld, J. I.; Francisco, J. S.; Hase, W. L. *Chemical Kinetics and Dynamics*; Prentice Hall: Upper Saddle River, NJ, 1998.

(48) (a) Joly, A. G.; Nelson, K. A. *Chem. Phys.* **1991**, *152*, 69–82. (b) Simon, J. D.; Xie, X. *J. Phys. Chem.* **1987**, *91*, 5538–5540.

(49) Paterson, M.; Hunt, P.; M.A., R.; Takahashi, O. *J. Phys. Chem. A* **2002**, *106*, 10494–10504.

**Table 1.** Peak Assignments and Dynamics for Experimentally Observed Species with Relative Intensities Given in Parentheses

species	BP86 DFT (cm <sup>-1</sup> )	lit. (cm <sup>-1</sup> )	exptl (cm <sup>-1</sup> )	time constant	trend
Cp*W(CO) <sub>3</sub> (Bpin)	1899 (1.0)	1900 <sup>g</sup>	1899 (s)	29 ± 12 ps <sup>e</sup>	rise <sup>e</sup>
	1917 (0.69)	1916 <sup>g</sup>	1914 (m)	213 ± 71 ps <sup>f</sup>	rise <sup>f</sup>
	1978 (0.67)	1999 <sup>g</sup>	2000 (s)	dynamics obscured by the 1931 cm <sup>-1</sup> peak	dynamics obscured by the 1931 cm <sup>-1</sup> peak
				36 ± 12 ps <sup>e</sup>	rise <sup>e</sup>
				222 ± 80 ps <sup>f</sup>	rise <sup>f</sup>
<i>cis</i> -Cp*W(CO) <sub>2</sub> (Bpin)(C <sub>5</sub> H <sub>12</sub> ) <sup>a</sup> (σ-alkane(1))(cis-σ-alkane)	1862 (1.0)	N/A	1844 (s)	21 ± 8.4 ps <sup>e</sup>	rise <sup>f</sup>
				247 ± 62 ps <sup>e</sup>	decay <sup>f</sup>
	1918 (0.96) <sup>d</sup>			13 ± 2 μs	decay
				dynamics obscured by the 1914 cm <sup>-1</sup> bleach	dynamics obscured by the 1914 cm <sup>-1</sup> bleach
Cp*W(CO) <sub>2</sub> (HBpin)(C <sub>5</sub> H <sub>11</sub> ) <sup>a</sup> (Int(1)/Bpin-back)	1761 (0.12) <sup>c</sup>	N/A		not observable due to low intensity	
	1864 (1.0)		1859 (s)	20 ± 3 μs	rise
				191 ± 39 μs	decay
	1934 (0.97)		1942 (m)	21 ± 4 μs	rise
				196 ± 71 μs	decay
Cp*W(CO) <sub>2</sub> (H) (Product(1))	1841 (0.2)	N/A	1820 (w)	dynamics obscured due to low intensity	
	1877 (1.0)		1835 (s)	166 ± 17 μs	rise
	1931 (1.0)		1932 (w) <sup>d</sup>	131 ± 33 μs	rise
<i>trans</i> -Cp*W(CO) <sub>2</sub> (Bpin)(C <sub>5</sub> H <sub>12</sub> ) <sup>b</sup> or Cp*W(CO) <sub>2</sub> (κ <sup>2</sup> -Bpin)(C <sub>5</sub> H <sub>12</sub> ) <sup>b</sup> (σ-alkane(2))	1856 <sup>g</sup> (1.0)	1867 <sup>h</sup> (1.0)	1852 (m)	26 ± 13 ps <sup>e</sup>	rise <sup>e</sup>
				190 ± 56 ps <sup>f</sup>	decay <sup>f</sup>
				7 ± 2 μs	decay
	1917 <sup>g</sup> (0.45)	1926 <sup>h</sup> (0.87)	1932 (m)	dynamics obscured by the 1914 cm <sup>-1</sup> bleach	dynamics obscured by the 1914 cm <sup>-1</sup> bleach
				5 ± 1 μs	decay
(Product(2))	1839	N/A	1828 (m)	6 ± 2 μs	rise
Cp*W(CO) <sub>3</sub> •	1895 (1.0)	1887 <sup>43</sup>	1888	147 ± 17 ps <sup>f</sup>	decay <sup>f</sup>
	1900 (0.66)				
	1965 (0.63)	1984 <sup>43</sup>	1978	4.5 ± 1 ps <sup>e</sup>	rise <sup>e</sup>
				229 ± 8.3 ps <sup>f</sup>	decay <sup>f</sup>

<sup>a</sup> BP86 DFT results correspond to a structure in which a propane molecule is substituted for pentane used experimentally. <sup>b</sup> BP86 DFT results correspond to a structure in which a methane molecule is substituted for pentane used experimentally. <sup>c</sup> W–H stretch. <sup>d</sup> Peak is partially obscured by the neighboring bleach (1914 cm<sup>-1</sup>). <sup>e</sup> Dynamics due to vibrational cooling. <sup>f</sup> Dynamics due to geminate recombination with photodissociated ligand. <sup>g</sup> *trans*-Cp\*W(CO)<sub>2</sub>(Bpin)(CH<sub>4</sub>) DFT calculated CO stretching modes (See Figure 10A). <sup>h</sup> Cp\*W(CO)<sub>2</sub>(κ<sup>2</sup>-Bpin)(CH<sub>4</sub>) DFT calculated CO stretching modes (See Figure 10B).

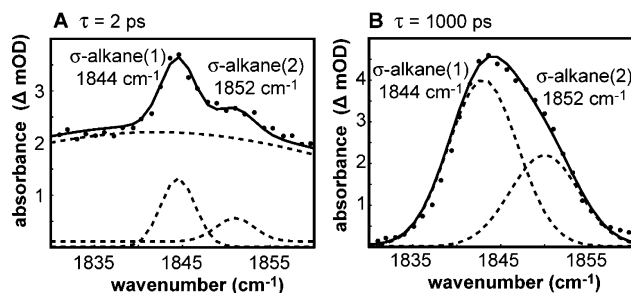


**Figure 3.** Enlargement of the feature attributed to Cp\*W(CO)<sub>2</sub>(Bpin)-(C<sub>5</sub>H<sub>12</sub>) at time delays of (A) 2 ps and (B) 1000 ps. The solid line corresponds to a fit of the data to multiple Lorentzian functions, which are shown individually as dashed lines. The broad Lorentzian in (A) is an adjustment to the baseline to account for vibrationally excited species and is not needed for spectra measured at time delays ( $\tau$ ) greater than ca. 30 ps.

The data and fits to the data clearly show a large peak at 1844 cm<sup>-1</sup> and a shoulder at 1852 cm<sup>-1</sup>. We propose that the two peaks correspond to two different isomers of Cp\*W(CO)<sub>2</sub>(Bpin)(C<sub>5</sub>H<sub>12</sub>), denoted  $\sigma$ -alkane(1) and  $\sigma$ -alkane(2). The two peaks show similar dynamics on the picosecond time scale, an average fast rise of 24 ± 11 ps and an average slow decay of 219 ± 59 ps (refer to Table 1 for the dynamics of the individual features). The fast rise is due to vibrational cooling, and the slow decay, which is in good agreement with the rise of the parent bleaches, is assigned to geminate recombination between the coordinatively unsaturated metal complex and the CO ligand. There is still significant

population of  $\sigma$ -alkane(1) and  $\sigma$ -alkane(2) after the slow decay, and the peak intensities do not change further between 500 ps and 3 ns.

These particular  $\sigma$ -alkane structures have not previously been observed experimentally. However, past DFT studies have indicated that the *cis*- $\sigma$ -alkane isomer is the first intermediate on the pathways to C–H bond cleavage.<sup>8,11,12</sup> Thus, we propose that one of the structures corresponds to *cis*-Cp\*W(CO)<sub>2</sub>(Bpin)(C<sub>5</sub>H<sub>12</sub>) and the other is an isomer of this  $\sigma$ -alkane complex. The reactions of these species occurring on the nano- through microsecond time scales are described in the following sections.

In summary, the picosecond time-resolved IR spectra of Cp\*W(CO)<sub>3</sub>(Bpin) in neat pentane solution show that irradiation of the starting material leads to the photodissociation of either •Bpin or CO to form Cp\*W(CO)<sub>3</sub>• or Cp\*W(CO)<sub>2</sub>(Bpin), respectively. Cp\*W(CO)<sub>3</sub>• recombines with the •Bpin to re-form the reactant within 200 ps. Cp\*W(CO)<sub>2</sub>(Bpin) is solvated by a pentane molecule from the bath within 2 ps to form two isomers of Cp\*W(CO)<sub>2</sub>(Bpin)(C<sub>5</sub>H<sub>12</sub>); neither  $\sigma$ -alkane isomer reacts on the picosecond time scale.

**3.2. Nanosecond and Microsecond Dynamics.** Figure 4 shows step-scan FTIR spectra of Cp\*W(CO)<sub>3</sub>(Bpin) in neat pentane

(50) The kinetic traces for the both  $\sigma$ -alkane isomers were determined by fitting a narrow peak area ( $\sigma$ -alkane(1) = 1844–1845 cm<sup>-1</sup> and  $\sigma$ -alkane(2) = 1851–1852 cm<sup>-1</sup>) plotted as a function of time to a single exponential function in order to extract separate time constants for the  $\sigma$ -alkane(1) and (2) isomers. The peak area of the entire feature, encompassing both the  $\sigma$ -alkane(1) and (2) peaks, plotted as a function of time is best fit to a biexponential function, indicating that the decays of the  $\sigma$ -alkane(1) and (2) peaks are separate kinetic events.

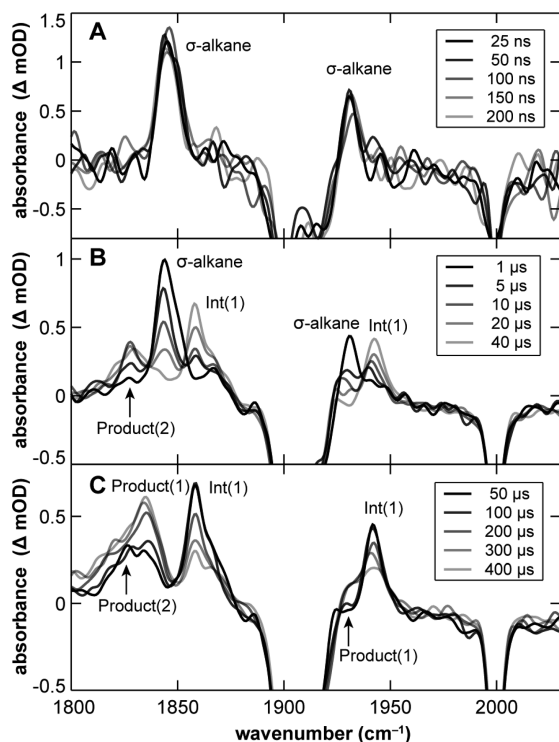


**Figure 4.** Nano- through microsecond step-scan FTIR spectra of  $\text{Cp}^*\text{W}(\text{CO})_3(\text{Bpin})$  in neat pentane solution with time delays between (A) 25 and 200 ns, (B) 1 and 40  $\mu\text{s}$ , and (C) 50 and 400  $\mu\text{s}$ . The parent bleaches have been omitted since they do not have dynamics on these time scales. The label Int(1), Product(1), and Product(2) refer to the intermediate and product species that are formed from  $\sigma$ -alkane(1) and  $\sigma$ -alkane(2). A detailed discussion of these reaction mechanisms is presented in section 4.

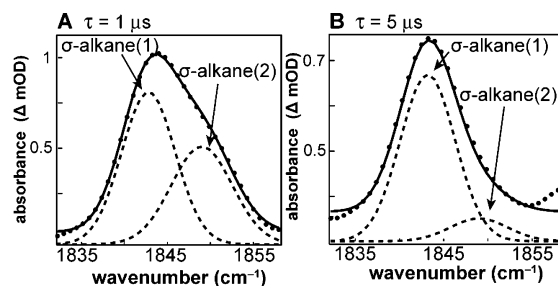


**Figure 5.** Enlargement of the feature attributed to  $\text{Cp}^*\text{W}(\text{CO})_2(\text{Bpin})$ -(pentane) at time delays of (A) 1  $\mu\text{s}$  and (B) 5  $\mu\text{s}$ . The solid line corresponds to a fit of the data to multiple Lorentzian functions, which are shown individually as dashed lines.

solution measured on the nano- through microsecond time scales. The spectra at time delays between 25 and 200 ns are displayed in Figure 4A. The peaks assigned to the  $\sigma$ -alkane complex are the only observable features in the spectra, and again, the 1844  $\text{cm}^{-1}$  feature is asymmetric, an indication that it consists of two peaks. The peaks assigned to the  $\sigma$ -alkane complexes exhibit no dynamics on the time scale shown in Figure 4A. The spectra at time delays from 1 to 40  $\mu\text{s}$  are displayed in Figure 4B. The peaks assigned to the  $\sigma$ -alkane complexes decay on this time scale. Panels A and B in Figure 5 show an enlargement of this feature at time delays of 1 and 5  $\mu\text{s}$ , respectively, along with a fit of the features to Lorentzian functions. The 1  $\mu\text{s}$  spectrum clearly shows an asymmetric band shape resulting from a large feature at 1844  $\text{cm}^{-1}$  and a shoulder at 1852  $\text{cm}^{-1}$ . The asymmetric line shape changes as a function of time and is no longer observable in the 5  $\mu\text{s}$  spectra. As shown in Figure 5B, the peak assigned as  $\sigma$ -alkane(2) on the blue side of the feature (1852  $\text{cm}^{-1}$ ) has decayed, leaving only the peak assigned as  $\sigma$ -alkane(1) (1844  $\text{cm}^{-1}$ ). Kinetic plots on the red and blue sides

of the feature are shown in Figure 6A,B, respectively. The peak assigned to the  $\sigma$ -alkane(1) complex at 1844  $\text{cm}^{-1}$  decays in  $13 \pm 2 \mu\text{s}$  (Figure 6A), and the peak from the  $\sigma$ -alkane(2) complex at 1852  $\text{cm}^{-1}$  decays in  $7 \pm 2 \mu\text{s}$  (Figure 6B).<sup>50</sup>

The spectra in Figure 4B also show three new peaks at 1828, 1859, and 1942  $\text{cm}^{-1}$ . The peaks at 1859 and 1942  $\text{cm}^{-1}$ , denoted Int(1), rise with time constants of  $20 \pm 3$  and  $21 \pm 4 \mu\text{s}$ , respectively, in reasonable agreement with the decay time constants of the  $\sigma$ -alkane(1) peak. A third peak, centered at 1828  $\text{cm}^{-1}$ , rises on a shorter time scale of  $6 \pm 2 \mu\text{s}$ , in agreement with the decay of the peak assigned to the  $\sigma$ -alkane(2) complex. The species corresponding to this peak undergoes no further reactions on the time scale of the experiment ( $<500 \mu\text{s}$ ) and is hereafter denoted Product(2). The kinetic plots for these species are displayed in Figure 6A,B. On the basis of the dynamics, it appears that  $\sigma$ -alkane(1) forms Int(1) in ca. 16  $\mu\text{s}$ , whereas  $\sigma$ -alkane(2) reacts to form Product(2) in 7  $\mu\text{s}$ . We propose that the  $\sigma$ -alkane(1)  $\rightarrow$  Int(1) pathway corresponds to the bond activation reaction, and the  $\sigma$ -alkane(2)  $\rightarrow$  Product(2) pathway corresponds to a side reaction that we discuss in detail in section 4.3.

Figure 4C shows spectra measured between 50 and 400  $\mu\text{s}$ . Two new features, appearing at 1835 and 1932  $\text{cm}^{-1}$ , are assigned to Product(1) because they persist throughout the remainder of this experiment (500  $\mu\text{s}$ ).<sup>51</sup> These features assigned to Product(1) do not agree with the reported CO stretching frequencies of  $[\text{Cp}^*\text{W}(\text{CO})_3]_2$  (1893 and 1920  $\text{cm}^{-1}$ )<sup>46</sup> or  $\text{Cp}^*\text{W}(\text{CO})_3(\text{H})$  (1924 and 2013  $\text{cm}^{-1}$ ).<sup>52</sup> An intermediate that has been observed on the micro- through millisecond time scale in past experiments.<sup>6</sup> Plots of the changes in the intensities of the peaks assigned to Product(1) and Int(1) plotted as a function of time are shown in Figure 7. The Int(1) peak at 1859  $\text{cm}^{-1}$  decays with a time constant of  $191 \pm 39 \mu\text{s}$ , and the Product(1) features rise on an average time scale of  $166 \pm 17 \mu\text{s}$ . The agreement of the time constants indicates that Int(1) forms Product(1) in 150–200  $\mu\text{s}$ . In the following sections, we present DFT calculations that allow for the assignment of the spectral features and dynamic processes observed experimentally.

#### 4. DFT Computational Modeling of Alkane C–H Bond Activation by $\text{Cp}^*\text{W}(\text{CO})_2(\text{Bpin})$

We have utilized DFT calculations to identify the complexes that correspond to the peaks described in section 3; the analysis herein focuses on the two mechanisms that have been proposed for alkane functionalization by transition-metal–boryl catalysts,  $\sigma$ -bond metathesis to form a metal–alkyl intermediate, and oxidative addition to form an alkyl hydride species (refer to Scheme 1). The results of these DFT calculations (refer to Table 2), when compared to the experiment, lend considerable insight into the bond activation mechanism. We present the  $\sigma$ -bond metathesis and oxidative addition mechanisms with the lowest computed values of the Gibbs free energy of activation ( $\Delta^\ddagger G$ ); alternate computed pathways are presented in the Supporting Information. Both mechanisms presented herein exclusively involve transient species in which the CO ligands are coordinated *cis* to each other. Our computational work shows that the reaction pathways in which transient species contain CO ligands coordinated *trans* to each other have Gibbs free energies of activation ( $\Delta^\ddagger G$ ) that are 5–15 kcal/mol higher in energy. The higher computed values for the Gibbs free energy of activation result from the significant geometric changes that must occur to bring the Bpin ligand and the alkyl group in proximity to one another in a *trans* geometry.

(51) While Product(1) is the final species observed here, it will ultimately react to form a more stable species,  $[\text{Cp}^*\text{W}(\text{CO})_3]_2$ .

(52) Kazlauskas, R. J.; Wrighton, M. S. *J. Am. Chem. Soc.* **1982**, *104*, 6005–6015.



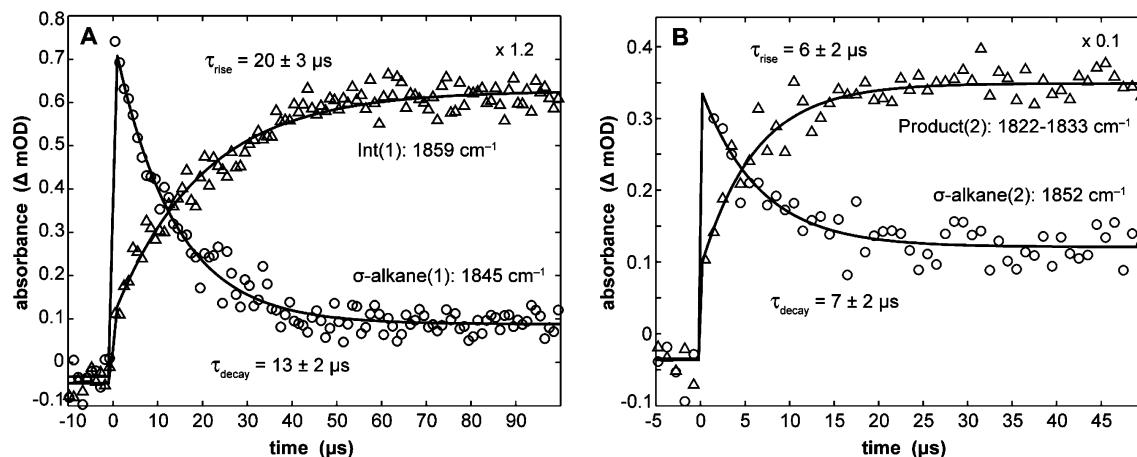


**Figure 6.** Kinetic plots for (A) the decay of the  $\sigma$ -alkane(1) peak (1845  $\text{cm}^{-1}$ ) and the rise of the Int(1) peak (1859  $\text{cm}^{-1}$ ) and (B) the decay of the  $\sigma$ -alkane(2) peak (1852  $\text{cm}^{-1}$ ) and the rise of the Product(2) peak (1828  $\text{cm}^{-1}$ ). The intensities of the Int(1) and Product(2) features are multiplied by 1.2 and 0.1, respectively, so that they are on a similar scale as the  $\sigma$ -alkane(1) and (2) features.

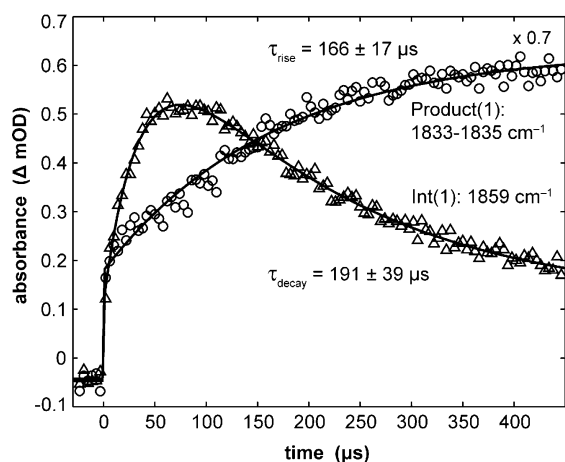


**Figure 7.** Kinetic plots for the decay of the Int(1) peak (1859  $\text{cm}^{-1}$ ) and the rise of the Product(1) peak (1835  $\text{cm}^{-1}$ ). The intensities of the Product(1) feature are multiplied by 0.7 so that it is on the same scale as the Int(1) feature.

**4.1.  $\sigma$ -Bond Metathesis Mechanism.** We have found that the pathway with the lowest computed values of the Gibbs free energy of activation for the borylation of propane by  $\text{Cp}^*\text{W}(\text{CO})_2(\text{Bpin})$  is the  $\sigma$ -bond metathesis mechanism depicted in Figure 8. In agreement with past DFT studies,<sup>11</sup> the first key intermediate in the mechanism is the *cis*- $\sigma$ -alkane complex, *cis*- $\text{Cp}^*\text{W}(\text{CO})_2(\text{Bpin})(\text{propane})$ . Because the dynamics described above indicate that the  $\sigma$ -alkane(1) peak corresponds to the first species in the bond activation reaction, we have assigned  $\sigma$ -alkane(1) to this *cis* isomer ( $\sigma$ -alkane(1) will now be referred to as *cis*- $\sigma$ -alkane). The kinetics in Figure 6 show that *cis*- $\sigma$ -alkane reacts to form Int(1) in ca. 16  $\mu\text{s}$ . As depicted in Figure 8, a saturated C–H bond on the alkane ligand in *cis*- $\sigma$ -alkane is cleaved by migration of the hydrogen atom to the Bpin ligand to generate a  $\sigma$ -borane complex in which the H atom and the propane ligand are adjacent (hereafter referred to as Bpin-back). The calculated Gibbs free energy of activation ( $\Delta^\ddagger G$ ) for this reaction ( $\text{TS1}_{\sigma\text{BM}}$ ) is 11.1 kcal/mol, which corresponds to a 22  $\mu\text{s}$  time constant by transition state theory.<sup>47</sup> This time constant is in good agreement with the 16  $\mu\text{s}$  decay of *cis*- $\sigma$ -alkane.<sup>53</sup> The calculated CO stretching modes of Bpin-back (1865 and 1941  $\text{cm}^{-1}$ ) are also in agreement with the peaks assigned to the IR stretching modes of Int(1) (1859 and 1942  $\text{cm}^{-1}$ ). The agreement of both the calculated frequencies and time constants

with the experimental values strongly supports the assignment of Int(1) as Bpin-back.

Past experimental studies predict that alkylboronate ester,  $\text{Cp}^*\text{W}(\text{CO})_2(\text{alkyl-Bpin})$ , is the final product of the bond activation reaction.<sup>6,9–11</sup> It is not possible to form this product directly from Bpin-back because the B atom is distal to the alkyl ligand,<sup>8,11</sup> and the complex must rearrange before the B–C bond can form. Thus, the next step in the reaction is calculated to be the rotation of the borane ligand to bring the boron and carbon atoms into close proximity. Figure 8 shows that the first rotation leads to a structure in which the Bpin ligand is adjacent to the  $\text{C}_3\text{H}_7$  group (Bpin-front). From Bpin-front, the formation of a B–C bond is facile because the boron and metal-bound alkyl carbon atoms are close to each other ( $\text{B–C} = 2.47 \text{ \AA}$ ). This B–C bond-forming process generates a complex containing an alkylboronate ligand,  $\text{Cp}^*\text{W}(\text{CO})_2(\text{H})(\text{H}_7\text{C}_3\text{-Bpin})$ . We do not expect to observe this alkylboronate complex in the experiment because the interaction between the tungsten and the alkyl-Bpin ligand is weak, and the alkyl-Bpin ligand would be expected to readily dissociate to form the free boronate ester and  $\text{Cp}^*\text{W}(\text{CO})_2(\text{H})$  ( $\text{TS5} = 0.8 \text{ kcal/mol}$ ).

A coarse-grained look at Figure 8 shows that there are two transition state structures,  $\text{TS1}_{\sigma\text{BM}}$  and  $\text{TS2}_{\sigma\text{BM}}$ , that might correspond to processes that are observable on the nano- through microsecond time scale. The first ( $\text{TS1}_{\sigma\text{BM}}$ ), as discussed earlier, corresponds to the reaction from *cis*- $\sigma$ -alkane to Bpin-back on a time scale of 16  $\mu\text{s}$ . We propose that the second transition state, connecting Bpin-back and Bpin-front ( $\text{TS2}_{\sigma\text{BM}}$ ), is the rate-limiting step in the remainder of the reaction, which is attributed to the 170  $\mu\text{s}$  time constant observed for the conversion of Int(1) to Product(1). By transition state theory, this experimentally observed time constant corresponds to a Gibbs free energy of activation ( $\Delta^\ddagger G$ ) of 12.3 kcal/mol. However, the calculated Gibbs free energy of activation for the Bpin-back to Bpin-front step ( $\text{TS2}_{\sigma\text{BM}}$ ) is 8.7 kcal/mol. This difference could be an artifact from the DFT results caused by our use of propane rather than pentane as the alkane in the bond activation reaction. The pentyl groups should experience greater steric interaction with the boryl ligand compared to the propyl groups, possibly explaining the discrepancy.

(53) All time constants presented in this publication ( $\tau$ ) are defined as  $\text{k}^{-1}$ . All Gibbs free energies of activation reported correspond to the Gibbs free energy of activation  $\Delta^\ddagger G$  calculated from transition state theory.

**Table 2.** Energies, Enthalpies, and Gibbs Free Energies of the Optimized Structures and Transition States Calculated Using the B3LYP Functional, and Frequencies of the Optimized Structures Calculated Using the BP86 Functional (Energy, Enthalpies, and Gibbs Free Energies (kcal/mol) Are Relative to *cis*-Cp\*W(CO)<sub>2</sub>(Bpin)(R) (R = CH<sub>4</sub> or C<sub>3</sub>H<sub>8</sub>), and Relative Intensities Are Given in Parentheses)

species <sup>a</sup>	B3LYP			BP86
	$\Delta E/\Delta E^\ddagger$	$\Delta H/\Delta H^\ddagger$	$\Delta G/\Delta G^\ddagger$	frequency (cm <sup>-1</sup> )
Cp*W(CO) <sub>2</sub> (Bpin)(C <sub>3</sub> H <sub>8</sub> ) <i>cis</i> - $\sigma$ -alkane	0.0	0.0	0.0	1862 (1.0) 1918 (0.96)
Cp*W(CO) <sub>2</sub> (Bpin)(C <sub>3</sub> H <sub>8</sub> ) $\rightarrow$ Cp*W(CO) <sub>2</sub> (HBpin)(C <sub>3</sub> H <sub>7</sub> ) <i>cis</i> - $\sigma$ -alkane $\rightarrow$ Bpin-back (TS1 <sub>oBM</sub> )	12.0	9.3	11.1	N/A
Cp*W(CO) <sub>2</sub> (HBpin)(C <sub>3</sub> H <sub>7</sub> ) Bpin-back	2.6	1.7	3.5	1761 (0.12) 1864 (1.0) 1934 (0.97)
Cp*W(CO) <sub>2</sub> (HBpin)(C <sub>3</sub> H <sub>7</sub> ) $\rightarrow$ Cp*W(CO) <sub>2</sub> (HBpin)(C <sub>3</sub> H <sub>7</sub> ) Bpin-back $\rightarrow$ Bpin-front (TS2 <sub>oBM</sub> )	13.0	11.4	12.2	N/A
Cp*W(CO) <sub>2</sub> (HBpin)(C <sub>3</sub> H <sub>7</sub> ) Bpin-front	11.4	10.3	10.0	1853 (0.20) <sup>b</sup> 1882 (0.63) 1937 (1.0)
Cp*W(CO) <sub>2</sub> (HBpin)(C <sub>3</sub> H <sub>7</sub> ) $\rightarrow$ Cp*W(CO) <sub>2</sub> (HBpin)(C <sub>3</sub> H <sub>7</sub> ) Bpin-front $\rightarrow$ Cp*W(CO) <sub>2</sub> (H)(H <sub>7</sub> C <sub>3</sub> -Bpin) (TS4 <sub>oBM</sub> )	8.8	6.6	9.8	N/A
Cp*W(CO) <sub>2</sub> (H <sub>7</sub> C <sub>3</sub> -Bpin)	-1.0	-2.8	-3.1	1851 (0.28) 1883 (1.0)
Cp*W(CO) <sub>2</sub> (H)(H <sub>3</sub> C-Bpin) $\rightarrow$ Cp*W(CO) <sub>2</sub> (H) (TS5)	4.3	1.9	0.8	N/A
Cp*W(CO) <sub>2</sub> (H)	-2.39	2.09	-10.2	1841 (0.2) <sup>b</sup> 1877 (1.0) 1931 (1.0)
Cp*W(CO) <sub>2</sub> (Bpin)(CH <sub>4</sub> ) $\rightarrow$ Cp*W(CO) <sub>2</sub> (Bpin)(H)(CH <sub>3</sub> ) <sup>c</sup> <i>cis</i> - $\sigma$ -alkane $\rightarrow$ Ox-Add (TS1 <sub>oA</sub> )	14.9	12.3	14.0	N/A
Cp*W(CO) <sub>2</sub> (Bpin)(H)(CH <sub>3</sub> ) <sup>c</sup> Ox-Add	4.98	3.44	4.94	1922 (0.08) <sup>b</sup> 1927 (1.0) 1974 (0.8)
Cp*W(CO) <sub>2</sub> (Bpin)(H)(CH <sub>3</sub> ) $\rightarrow$ Cp*W(CO) <sub>2</sub> (HBpin)(CH <sub>3</sub> ) <sup>c</sup> Ox-Add $\rightarrow$ Bpin-up (TS2 <sub>oA</sub> )	4.95	2.56	6.32	N/A
Cp*W(CO) <sub>2</sub> (HBpin)(CH <sub>3</sub> ) <sup>c</sup> Bpin-up	2.85	1.63	3.98	1791 (0.05) <sup>b</sup> 1917 (0.97) 1964 (1.0)
Cp*W(CO) <sub>2</sub> (HBpin)(CH <sub>3</sub> ) $\rightarrow$ Cp*W(CO) <sub>2</sub> (HBpin)(CH <sub>3</sub> ) <sup>c</sup> Bpin-up $\rightarrow$ Bpin-front (TS3)	7.69	6.51	9.79	N/A
Cp*W(CO) <sub>2</sub> ( $\kappa^2$ -Bpin)(CH <sub>4</sub> ) <sup>c</sup> (Figure 10B)	1.58	1.05	-2.5	1867 (1.0) 1926 (0.87)
<i>trans</i> -Cp*W(CO) <sub>2</sub> (Bpin)(CH <sub>4</sub> ) <sup>c</sup> <i>trans</i> - $\sigma$ -alkane (Figure 10A)	1.11	0.43	3.0	1856 (1.0) 1917 (0.45)

<sup>a</sup> Refer to Figures 8, 9 and 10. <sup>b</sup> W–H stretch. <sup>c</sup> Energies, enthalpies, and Gibbs free energies set relative to *cis*-Cp\*W(CO)<sub>2</sub>(Bpin)(CH<sub>4</sub>) rather than *cis*-Cp\*W(CO)<sub>2</sub>(Bpin)(C<sub>3</sub>H<sub>8</sub>).

To test this hypothesis, we performed DFT calculations of the borylation of methane by Cp\*W(CO)<sub>2</sub>(Bpin). If the propane moiety hinders the rotation of the H-Bpin ligand more than the methane moiety does, the Gibbs free energy of activation will be lower for the methane borylation reaction. As occurs during the mechanism for functionalization of propane, after the formation of Bpin-back in the methane borylation reaction, the H–Bpin ligand rotates to bring the Bpin and alkyl ligands close to each other. However, for the methane borylation reaction, the calculated Gibbs free energy of activation associated with the rotation reaction is 6.4 kcal/mol, which is 2.3 kcal/mol lower in energy than the analogous transition state in the functional-

ization of propane. These calculations indicate that the Gibbs free energy of activation for the functionalization of propane agrees better with experiment than those for the functionalization of methane.<sup>54</sup> Thus, the discrepancy between the experiment and the calculations presented in Figure 8 could be attributed to the use of propane in the DFT-calculated reaction rather than pentane, the solvent used in the experiments.<sup>54</sup> We believe that a DFT calculation using pentane would have a barrier similar to our experiment; however, calculating the reaction using a larger alkane is not practical because of the many conformations of the pentyl chain.



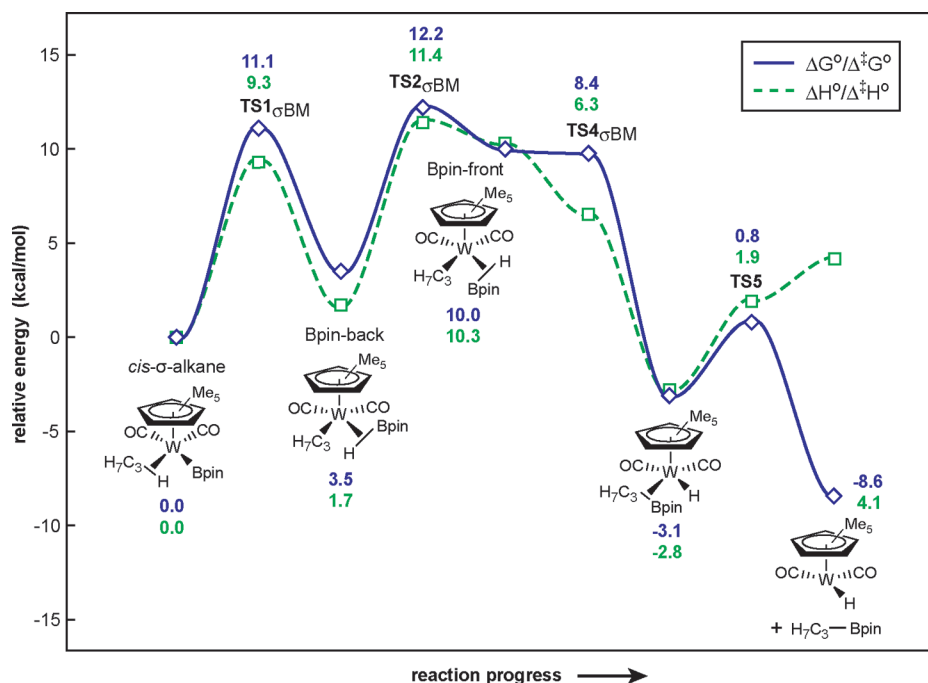


**Figure 8.**  $\sigma$ -Bond metathesis mechanism for the borylation reaction of propane as calculated by DFT. Enthalpies and Gibbs free energies (kcal/mol) are relative to *cis*-Cp\*W(CO)<sub>2</sub>(Bpin)(C<sub>3</sub>H<sub>8</sub>).

Because both of the intermediates between Bpin-back and Cp\*W(CO)<sub>2</sub>(H) in Figure 8 are calculated to be so short-lived that they would not be observable on the microsecond time scale, the peaks in Figure 4C (1835 and 1932 cm<sup>-1</sup>) labeled Product(1) are assigned to Cp\*W(CO)<sub>2</sub>(H). The observed Product(1) peaks are in partial agreement with the calculated CO stretching modes for this complex (1877 and 1931 cm<sup>-1</sup>).<sup>55</sup> Cp\*W(CO)<sub>2</sub>(H) will eventually react to form either Cp\*W(CO)<sub>3</sub>(H) or [Cp\*W(CO)<sub>3</sub>]<sub>2</sub> by collision with free CO or a Cp\*W(CO)<sub>2</sub>(H) fragment, respectively.<sup>6,9,10</sup> While we do not observe the formation of these complexes on the microsecond time scale, they have been observed as final products in past experimental investigations.<sup>6,8–10</sup>

**4.2. Oxidative Addition Mechanism.** Although the evidence for the  $\sigma$ -bond metathesis mechanism as outlined in section 4.1 is compelling, we also assessed the energies of intermediates in the alternative oxidative addition mechanism. Oxidative addition mechanisms are more common for C–H bond functionalization reactions catalyzed by mid-to-late transition-metal

compounds.<sup>1,13</sup> In the case of transition-metal–boryl compounds, the highest yields for stoichiometric and catalytic borylation of aliphatic C–H bonds are observed with complexes of tungsten and rhodium, respectively, and for this reason, the oxidative addition mechanism was originally favored.<sup>9</sup>

We have performed DFT calculations for selected intermediates and transition states in a proposed mechanism for oxidative addition of CH<sub>4</sub> by Cp\*W(CO)<sub>2</sub>(Bpin) using DFT calculations. The oxidative addition pathway with the lowest Gibbs free energy of activation is depicted in Figure 9. The reaction begins with the *cis*- $\sigma$ -alkane complex; but in this case, the first step is insertion of the tungsten center into a C–H bond of CH<sub>4</sub> to form the alkyl hydride complex, Cp\*W(CO)<sub>2</sub>(Bpin)(H)(CH<sub>3</sub>). The calculated Gibbs free energy of activation associated with this process (TS1<sub>OA</sub>) is 4.2 kcal/mol higher than that of the corresponding step in the  $\sigma$ -bond metathesis mechanism for the activation of methane. The time constant for the reaction, as predicted by transition state theory, is 3 ms, and this value is roughly 3 orders of magnitude slower than the 16  $\mu$ s time constant observed experimentally. The transition state for oxidative addition of the primary C–H bond of propane is also higher in energy than the  $\sigma$ -bond metathesis transition state for propane activation, TS1<sub>σBM</sub> (for TS1<sub>OA</sub>, propane,  $\Delta^{\ddagger}H$  = 13.6 kcal/mol and  $\Delta^{\ddagger}G$  = 15.2 kcal/mol; therefore,  $\Delta\Delta^{\ddagger}G$  = 4.1 kcal/mol). The next step is the formation of a B–H bond between the Bpin and the hydride ligand, creating a  $\sigma$ -borane complex with the axis of the Bpin ligand parallel to the W–Cp\* (centroid) axis and the hydrogen closer than the boron atom to the Cp\* ligand (Bpin-up). In a similar fashion to the rearrangement in the  $\sigma$ -bond metathesis mechanism in Figure 8, the borane ligand rotates to place the boron and metal-bound alkyl carbon atoms close to each other. From this point forward (TS4–TS5), the mechanisms in Figures 8 and 9 are identical.

If the reaction were to proceed via the oxidative addition mechanism, the feature labeled Int(1) in the infrared spectra would correspond to the alkyl hydride complex formed by

(54) The DFT-calculated results for the propane ligands indicate that  $\sigma$ -alkane will react to form Bpin-back with a Gibbs free energy of activation of 11.1 kcal/mol, 22  $\mu$ s by transition state theory. This is in excellent agreement with the 16  $\mu$ s decay of *cis*- $\sigma$ -alkane observed experimentally. However, DFT also predicts that Bpin-back is 3.5 kcal/mol less stable than *cis*- $\sigma$ -alkane and, thus, will not be observable experimentally. Under this interpretation, the Gibbs free energy of activation for the formation of Bpin-front corresponds to the energy difference between *cis*- $\sigma$ -alkane and TS2<sub>σBM</sub>, 12.2 kcal/mol, corresponding to a time constant of 139  $\mu$ s. Interestingly, this is in good agreement with the observed rate for the reaction of Int(1) to Product(1). However, it is also clear from experiment that a significant population of Int(1) (Bpin-back) is formed, and this is in poor agreement with the DFT results. There is not good agreement between the calculated energy of the Bpin-back local minimum and the fact that Bpin-back is observed experimentally.

(55) The CO stretching frequencies of Cp\*W(CO)<sub>2</sub>(H)(propane) have also been calculated but are only marginally different from the calculated frequency of Cp\*W(CO)<sub>2</sub>(H). It is unclear why the lower frequency peak observed experimentally is 40 cm<sup>-1</sup> lower in energy than predicted by DFT. It is possible that the discrepancy is due to the multiple isomers of the alkyl solvated species.

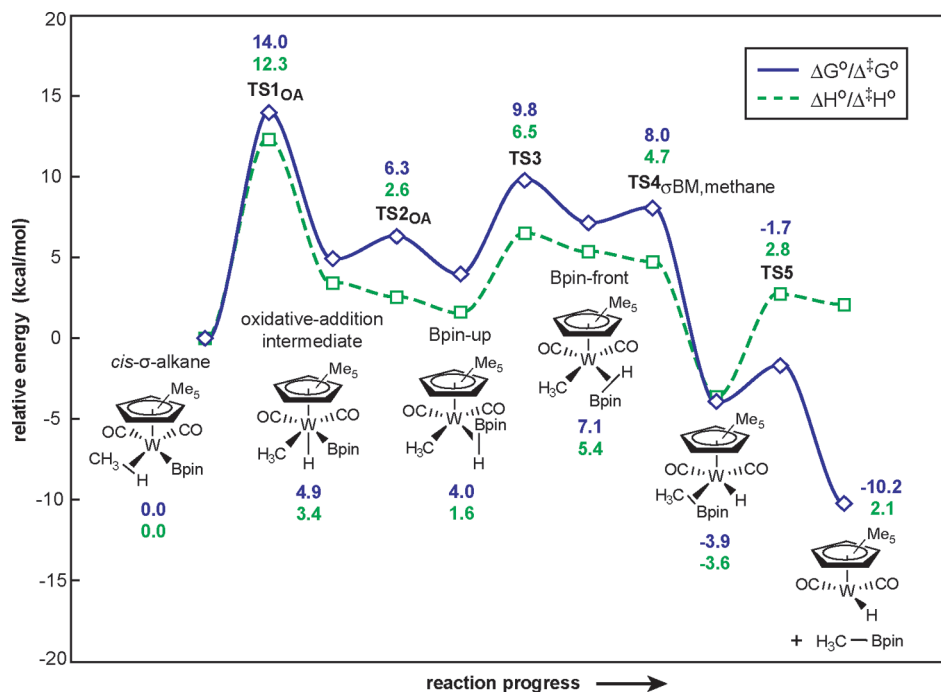
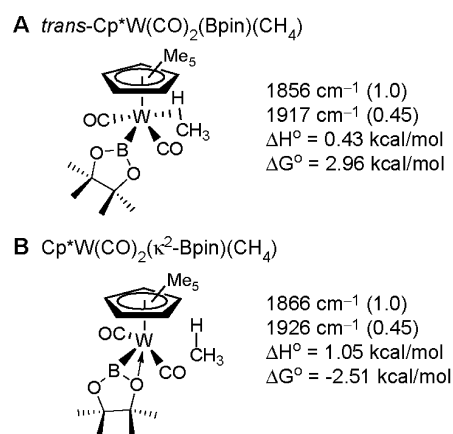


**Figure 9.** Oxidative addition mechanism for the activation of  $\text{CH}_4$  by  $\text{cis-Cp}^*\text{W}(\text{CO})_2(\text{Bpin})$  as calculated by DFT. Enthalpies and Gibbs free energies (kcal/mol) are relative to  $\text{cis-Cp}^*\text{W}(\text{CO})_2(\text{Bpin})(\text{CH}_4)$ . In this oxidative addition mechanism for C–H bond activation, there is still a  $\sigma$ -bond metathesis step ( $\text{TS4}_{\sigma\text{BM, methane}}$ ) for the production of bound product. Direct reductive elimination of  $\text{CH}_3\text{Bpin}$  from the oxidative-addition intermediate is higher in energy than the pathway calculated for the  $\sigma$ -bond metathesis step.

oxidative addition or to Bpin-up. The calculated CO stretching frequencies of neither Bpin-up ( $1917$  and  $1964\text{ cm}^{-1}$ ) nor the alkyl hydride complex ( $1927$  and  $1974\text{ cm}^{-1}$ ) agree with those measured experimentally ( $1859$  and  $1942\text{ cm}^{-1}$ ). The large discrepancies between the observed and calculated frequencies ( $\sim 60$  and  $\sim 30\text{ cm}^{-1}$  for the antisymmetric and symmetric modes, respectively) and the higher Gibbs free energy of activation calculated for  $\text{TS1}_{\text{OA}}$  argue strongly against reaction by the oxidative addition pathway.

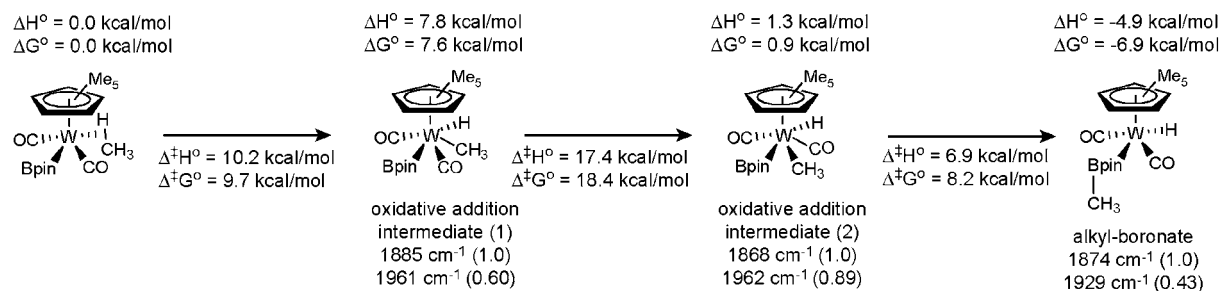
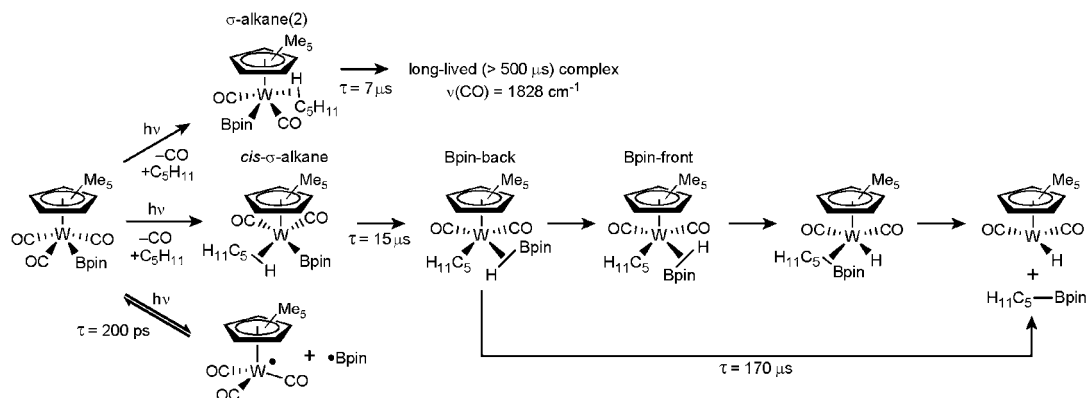
**4.3. Side Reactions.** The preceding analysis provides strong evidence in favor of the  $\sigma$ -bond metathesis mechanism in Figure 8. However, we also observe a side reaction that leads to the formation of Product(2) from  $\sigma$ -alkane(2) (refer to section 3.2). Unlike the radical side reaction discussed in section 3.1, the side reaction involving  $\sigma$ -alkane(2) and Product(2) yields relatively long-lived products that appear to cause the final yield of alkylboronate ester product to be less than quantitative. The  $\sigma$ -alkane(2) complex is discernible within 2 ps after photolysis and is likely to be an isomer of  $\text{Cp}^*\text{W}(\text{CO})_2(\text{Bpin})(\text{C}_5\text{H}_{12})$ .  $\sigma$ -Alkane(2) does not decay in concert with the appearance of a feature assigned to an intermediate in the functionalization process. Instead, it decays to form Product(2) in  $7\text{ }\mu\text{s}$ , and Product(2) is unreactive on the time scale of the experiment ( $<500\text{ }\mu\text{s}$ ).

All of the intermediates discussed to this point contain CO ligands in a *cis* geometry, and we propose that  $\sigma$ -alkane(2) corresponds to a different isomer. Figure 10 shows two isomers of  $\text{Cp}^*\text{W}(\text{CO})_2(\text{Bpin})(\text{CH}_4)$ . The simplest one is  $\text{trans-Cp}^*\text{W}(\text{CO})_2(\text{Bpin})(\text{C}_5\text{H}_{12})$  (Figure 10A). The calculated CO vibrational frequency of  $\text{trans-Cp}^*\text{W}(\text{CO})_2(\text{Bpin})(\text{CH}_4)$  ( $1856\text{ cm}^{-1}$ ) is in good agreement with the  $\sigma$ -alkane(2) peak ( $1852\text{ cm}^{-1}$ ). Alternatively, the Bpin ligand could be bound to tungsten in a  $\kappa^2$  fashion; in such a structure, there would be a strong covalent bond between the tungsten and the boron atoms ( $\text{W-B} = 2.14\text{ \AA}$ ) and a dative bond between the oxygen and the tungsten. In



**Figure 10.** Molecular structures for (A)  $\text{trans-Cp}^*\text{W}(\text{CO})_2(\text{Bpin})(\text{CH}_4)$  and (B)  $\text{Cp}^*\text{W}(\text{CO})_2(\kappa^2\text{-Bpin})(\text{CH}_4)$ . Enthalpies and Gibbs free energies are relative to  $\text{cis-Cp}^*\text{W}(\text{CO})_2(\text{Bpin})(\text{CH}_4)$ .

this  $\kappa^2$  structure, the alkane would be weakly associated with the metal complex through a van der Waals (dipole/induced dipole) interaction. In this structure, the two CO ligands, the alkane, and the Bpin ligand constitute the base of a four-legged structure (Figure 10B). The  $\kappa^2$ -bound structure lies at a minimum on the potential energy surface and is slightly more stable than the *trans*- $\sigma$ -bonded complex. Its vibrational frequency ( $1866\text{ cm}^{-1}$ ) is also in good agreement with the experiment ( $1852\text{ cm}^{-1}$ ). Ultimately, we cannot conclusively determine which of the two structures in Figure 10 corresponds to the  $\sigma$ -alkane(2) peak, and because the complexes are predicted to have nearly identical CO stretching frequencies and are similar in energy, both structures could contribute to the observed feature. Our DFT analysis does indicate that the  $\kappa^2$ -bound structure (Figure 10B) cannot directly activate a C–H bond; instead, it must first rearrange to either the *cis*- or the *trans*- $\sigma$ -alkane.

**Scheme 2.** DFT-Calculated Mechanisms for the Oxidative Addition Bond Activation Reaction of *trans*- $\sigma$ -Alkane**Scheme 3.** Experimentally Observed Photochemical Reactions of  $\text{Cp}^*\text{W}(\text{CO})_3(\text{Bpin})$  in Neat Pentane Solution, Including the C–H Bond Activation (Center) and Two Side Reactions (Top and Bottom)

The experimental data show that  $\sigma$ -alkane(2) converts into Product(2) on a time scale of 7  $\mu\text{s}$ . Only one feature centered at 1828  $\text{cm}^{-1}$  was observed for Product(2), most likely because the second band is obscured by one of the parent bleaches (refer to Table 1). There is little evidence in the literature for bond formation between two ligands located *trans* to each other in a four-legged piano stool geometry; we, nevertheless, investigated whether B–C bond formation could occur between *trans* alkyl and boryl ligands. Consistent with our expectations, the DFT calculations indicate that the conversion of the *trans*- $\sigma$ -alkane to  $\sigma$ -borane complex in this geometry has a high barrier due to the large distance between the B and H atoms (4.2 Å). Thus, the conversion of  $\sigma$ -alkane(2)  $\rightarrow$  Product(2) is unlikely to occur by a  $\sigma$ -bond metathesis reaction that converts an alkane complex to a borane complex and ultimately forms the B–C bond in the alkylboronate ester.

Scheme 2 shows a more viable oxidative addition pathway in which the intermediates contain mutually *trans* CO ligands. Here the tungsten is inserted into one of the alkane C–H bonds to form *trans*- $\text{Cp}^*\text{W}(\text{CO})_2(\text{Bpin})(\text{H})(\text{CH}_3)$ . In the following step, the  $\text{CH}_3$  ligand migrates so that it is in close proximity to the Bpin ligand. From this geometry, the alkyl-Bpin group is readily formed. The calculated Gibbs free energy of activation for the *trans*- $\text{Cp}^*\text{W}(\text{CO})_2(\text{Bpin})(\text{CH}_4)$  and *trans*- $\text{Cp}^*\text{W}(\text{CO})_2(\text{Bpin})(\text{H})(\text{CH}_3)$  step is 9.7 kcal/mol, corresponding to a time constant of 2.5  $\mu\text{s}$ , in good agreement with the observed 7  $\mu\text{s}$  time constant for the conversion of  $\sigma$ -alkane(2) to Product(2). However, neither of the calculated CO stretching modes for this complex (1885 and 1961  $\text{cm}^{-1}$ ) agree with the observed IR band labeled Product(2) (1828  $\text{cm}^{-1}$ ). Thus, Product(2) does not appear to be formed via an oxidative addition pathway in which the intermediates contain *trans* CO ligands.

Since the DFT calculations provide no evidence that the conversion of  $\sigma$ -alkane(2) to Product(2) involves C–H bond cleavage, we have investigated some ligand dissociation reac-

tions of the  $\sigma$ -alkane complexes in an attempt to identify a stable complex containing a CO stretch near 1828  $\text{cm}^{-1}$ . We have considered the possibility that Product(2) is due to  $\text{Cp}^*\text{W}(\text{CO})_2^*$ , which would be formed after the dissociation of  $\bullet\text{Bpin}$  from *trans*- $\sigma$ -alkane, but the W–B bond dissociation energy determined by DFT is ca. 71.0 kcal/mol, and the calculated CO stretching modes (1851 and 1908  $\text{cm}^{-1}$ ) agree poorly with the experimentally observed CO stretch near 1828  $\text{cm}^{-1}$ . The only species for which we calculate a CO stretching mode in the vicinity of 1828  $\text{cm}^{-1}$  contain a single CO ligand. Thus, we considered that Product(2) could form by dissociation of CO from a  $\sigma$ -alkane complex, even though it seemed unlikely that a  $\sigma$ -alkane isomer would dissociate a strongly bound CO ligand over a weakly bound alkane ligand. Consistent with our expectations, DFT calculations predict that the CO bond dissociation energy in the alkane complex is 54.2 kcal/mol,<sup>56</sup> indicating Product(2) is not accessible from  $\sigma$ -alkane(2) on the early microsecond time scale. It is possible that the CO dissociation occurs via a concerted solvent-assisted mechanism that would accelerate the dissociation rate, but this mechanism seems improbable because DFT calculations indicate that a second  $\text{CH}_4$  molecule does not stabilize  $\text{Cp}^*\text{W}(\text{CO})(\text{Bpin})(\text{CH}_4)$ . Ultimately, we cannot conclusively assign Product(2). However,

(56) This energy is similar to the CO bond dissociation energy for  $\text{Cp}^*\text{W}(\text{CO})_3(\text{Bpin})$ , which is calculated to be 53.2 kcal/mol.

(57) The branching ratio is estimated by analyzing the relative peak amplitudes of the antisymmetric CO stretching modes of *cis*- $\text{Cp}^*\text{W}(\text{CO})_2(\text{Bpin})(\text{C}_5\text{H}_{12})$  and *trans*- $\text{Cp}^*\text{W}(\text{CO})_2(\eta^2\text{-Bpin})(\text{C}_5\text{H}_{12})$ , the 1844 and 1852  $\text{cm}^{-1}$  peaks in Figure 3, respectively. The Lorentzian fit to these peaks (refer to Figure 3) indicates that the 1852  $\text{cm}^{-1}$  peak is 54% as intense as the 1844  $\text{cm}^{-1}$  peak. Throughout this analysis, we weigh the branching ratio by the DFT calculated oscillator strengths of the antisymmetric CO stretching modes for the two complexes. It should also be noted that this estimate does not account for the parent molecules that undergo geminate recombination with photodissociated CO ligands.



the spectroscopic data indicate that Product(2) does not add to the final yield of functionalized product.

On the basis of the experimentally observed peak intensities and the calculated oscillator strengths of the  $\sigma$ -alkane complexes, we calculated the effect of the  $\sigma$ -alkane(2) side reaction on the total bond activation yield.<sup>57</sup> We estimate that 35% of the reactant molecules that undergo photodissociation form  $\sigma$ -alkane(2). This complex reacts to form Product(2) in ca. 7  $\mu$ s, and this pathway does not contribute to the final C–H bond activation yield. The other 65% of the reactant molecules form *cis*- $\sigma$ -alkane. This complex follows the more favorable pathway depicted in Figure 8, resulting in the formation of the final functionalized product, H<sub>11</sub>C<sub>5</sub>-Bpin. This prediction is in accord with past studies on this complex, which report a C–H bond activation yield of 72%.<sup>6,9,10,57</sup> Thus, the yield observed experimentally is likely the result of an alternative  $\sigma$ -alkane structure formed within 2 ps after photolysis.

## 5. Conclusions

The results of the time-resolved IR studies conducted on the photoinduced reactions of Cp\*W(CO)<sub>3</sub>(Bpin) are summarized in Scheme 3. The primary reaction pathway, shown in the center row, begins with the photodissociation of CO from Cp\*W(CO)<sub>3</sub>(Bpin) and solvation of the metal complex by a pentane molecule, forming *cis*- $\sigma$ -alkane within 2 ps. *cis*- $\sigma$ -Alkane is then proposed to undergo a  $\sigma$ -bond metathesis reaction to cleave a primary C–H bond on the pentane ligand and form a B–H bond. To ultimately form a B–C bond, it is necessary for the borane ligand to rotate 180° to place the boron atom of the borane adjacent to the C<sub>5</sub>H<sub>11</sub> ligand. From this configuration, the B–C bond is calculated to form readily and to generate Cp\*W(CO)<sub>2</sub>(H)(H<sub>11</sub>C<sub>5</sub>-Bpin) containing a metal hydride and a coordinated alkylboronate. The H<sub>11</sub>C<sub>5</sub>-Bpin group is calculated to be weakly bound to the metal and to readily eliminate to form Cp\*W(CO)<sub>2</sub>(H) and the free functionalized product H<sub>11</sub>C<sub>5</sub>-Bpin. The rate-limiting step, occurring with a time constant of 170  $\mu$ s, is proposed to correspond to rotation of the borane ligand, generating a conformer in which the boron atom occupies a position adjacent to the C<sub>5</sub>H<sub>11</sub> ligand.

In addition to the major C–H bond functionalization process, we have observed two side reactions. Excitation at 266 nm leads to the photodissociation of the •Bpin radical to form Cp\*W(CO)<sub>3</sub>• (refer to the bottom pathway in Scheme 2). This radical pathway does not irreversibly consume the reactant because Cp\*W(CO)<sub>3</sub>• efficiently recombines with •Bpin to reform the reactant within 200 ps. The second side reaction has a larger influence on the total yield of functionalized products. The molecules involved in the side reaction are proposed to be geometric isomers of the intermediates involved in the functionalization process. The species that do not form the functionalized product are proposed to contain the boryl and alkyl group in positions *trans* to each other, increasing the barrier to C–H bond cleavage by  $\sigma$ -bond metathesis. Unfortunately, we cannot conclusively determine the identity of the product formed by this process.

This work represents the first spectroscopic detection of the key intermediates in a  $\sigma$ -bond metathesis mechanism for C–H

bond activation by tungsten–boryl complexes, a mechanism that is notably different from the C–H bond activation mechanisms followed by late transition-metal compounds.<sup>1,3,7,13</sup> High-valent early transition-metal complexes follow  $\sigma$ -bond metathesis mechanisms because these complexes cannot undergo oxidative addition.<sup>4,9</sup> This class of mechanism is less commonly followed by low-valent late transition-metal complexes, but related pathways have been computed for reactions of low-valent alkyl complexes with arenes.<sup>31,58</sup> The highest yields of functionalized products from the reactions of alkanes with boryl complexes contain third-row metal centers, such as tungsten. Thus, these compounds were initially expected to react via oxidative addition.<sup>4,7,9,29</sup> Data from past experimental and computational studies have suggested that this  $\sigma$ -bond metathesis mechanism is favorable because the electropositive nature of the boron reduces the barrier for cleaving the C–H bond and leads to a small barrier for forming a B–C bond.<sup>9,11,48,59</sup> These previous studies have also suggested that the slow step in the functionalization reaction is the cleavage of the C–H bond.<sup>9,11,48,59</sup> In contrast, the work presented here provides evidence that the highest energy transition state corresponds to the barrier for rotation of the borane ligand to place the boryl group adjacent to the alkyl ligand. Further spectroscopic and computational work is underway to determine if these conclusions apply to related metal–boryl complexes that are intermediates in reactions that functionalize alkanes catalytically.

**Acknowledgment.** This work was supported by the LBNL Laboratory Directed Research and Development program (LDRD: 3657-48) to C.B.H. and by the NSF (CHE-09-10641) to J.F.H. We also acknowledge some specialized equipment supported by the U.S. Department of Energy Office of Basic Energy Sciences, Chemical Sciences Division, under contract DE-AC02-05CH11231 and contractor supported research (CSR). Computational work was performed on resources at the University of Memphis High-Performance Computing Facility. J.F.C. acknowledges an NSF graduate research fellowship, and M.F.K. acknowledges a Feodor-Lynen fellowship by the Alexander von Humboldt foundation. Special thanks to Heinz Frei for use of the step-scan FTIR spectrometer.

**Supporting Information Available:** Discussion of minor side products in the bond activation reaction; ultrafast broadband IR-pump, IR-probe spectra of Cp\*W(CO)<sub>3</sub>(Bpin) in neat pentane solution; DFT-calculated methane C–H bond activation reaction by *cis*-Cp\*W(CO)<sub>2</sub>(Bpin); DFT-calculated higher energy  $\sigma$ -bond metathesis and oxidative addition C–H bond activation mechanisms; full citation for ref 21. This material is available free of charge via the Internet at <http://pubs.acs.org>.

JA906438A

- (58) (a) Lail, M.; Bell, C. M.; Conner, D.; Cundari, T. R.; Gunnoe, T. B.; Peterson, J. L. *Organometallics* **2004**, 23, 5007–5020. (b) Oлгаard, J.; Periana, R. A.; Goddard, W. A. *J. Am. Chem. Soc.* **2004**, 126, 11658–11665. (c) Vastine, B. A.; Hall, M. B. *Coord. Chem. Rev.* **2009**, 253, 1202–1218.
- (59) (a) Baker, R. T.; Calabrese, J. C. *J. Am. Chem. Soc.* **1993**, 115, 4367–4368. (b) Baker, R. T.; Calabrese, J. C.; Westcott, S. A.; Marder, T. B. *J. Am. Chem. Soc.* **1995**, 117, 8777–8784.